Febuxostat inhibits non-small cell lung cancer cell proliferation under starvation conditions by modulating xanthine oxidoreductase-associated autophagy

XIN-HUANG YAO[1], MING SHAO[1] and YI-WEI XU[2]

[1]Department of Central Laboratory, The Second Affiliated Hospital, School of Medicine, The Chinese University of Hong Kong, Shenzhen and Longgang District People's Hospital of Shenzhen, Shenzhen, Guangdong 518172, P.R. China; [2]Department of Clinical Laboratory Medicine, Esophageal Cancer Prevention and Control Research Center, Cancer Hospital of Shantou University Medical College, Shantou, Guangdong 515041, P.R. China

Received March 31, 2026; Accepted August 6, 2026

DOI: 10.3892/ol.2026.15925

Abstract. Febuxostat (FBX), a selective non-purine xanthine oxidoreductase (XOR) inhibitor clinically indicated for hyperuricemia, has recently attracted attention for its potential antitumor properties. Nevertheless, its potential therapeutic efficacy against non-small cell lung cancer (NSCLC) remains to be fully characterized. XOR expression and enzymatic activity were quantified in NSCLC lines (A549 and SK-MES-1) and compared with normal human bronchial epithelial BEAS-2B cells. The effects of XOR and FBX on cell proliferation, migration and invasion were evaluated using the cell counting kit-8, wound-healing and Matrigel-Transwell invasion assays, respectively. Apoptosis and autophagic flux under starvation conditions (FBS-free DMEM) were assessed using Annexin V/SYTOX staining, DCFH-DA, western blotting (p62 and LC3-II) and LysoTracker Red staining. The functional role of autophagy was validated through rescue experiments using the autophagy activator rapamycin. XOR was found to be markedly upregulated and hyperactive in NSCLC cells compared with normal epithelial cells. Small interfering RNA-mediated XOR knockdown attenuated NSCLC cell viability, migration and invasion. Pharmacological inhibition of XOR by FBX likewise impaired proliferative, migratory and invasive capacities, accompanied by marked suppression of autophagic flux. Notably, these antitumor effects were abrogated by rapamycin-induced autophagy activation. The present findings demonstrated that XOR is involved in the metabolic drive of NSCLC progression under nutrient-deprived conditions. Specifically, FBX exerted anticancer effects by blocking XOR-mediated pathways and suppressing protective autophagy, suggesting that repurposing FBX for NSCLC therapy warrants further preclinical investigation.

Correspondence to: Mr. Xin-Huang Yao, Department of Central Laboratory, The Second Affiliated Hospital, School of Medicine, The Chinese University of Hong Kong, Shenzhen and Longgang District People's Hospital of Shenzhen, 53 Aixin Road, Longgang, Shenzhen, Guangdong 518172, P.R. China
E-mail: yaoxinh@alumni.sysu.edu.cn

Key words: autophagy, autophagic flux, febuxostat, non-small cell lung cancer, xanthine oxidoreductase

Introduction

According to 2022 global cancer statistics, lung cancer remains the leading cause of oncological mortality, accounting for 12.5% all cases of cancer-related mortality worldwide (1). Lung cancer can be primarily classified into small cell lung cancer (SCLC) and non-SCLC (NSCLC). NSCLC represents ~85% of all cases and is associated with poor long-term survival (2,3). Histologically, NSCLC can be further categorized into lung adenocarcinoma (LUAD), lung squamous cell carcinoma (LUSC) and large cell carcinoma, with LUAD and LUSC collectively constituting 70% of all lung cancer diagnoses (4). Despite therapeutic advancements, evolving from conventional surgery and cytotoxic chemotherapy to targeted therapies and immunotherapies, the long-term prognosis for patients with advanced NSCLC remains poor, with 5-year overall survival (OS) rates historically at ~6% (2,5,6).

Autophagy is a conserved catabolic process essential for maintaining cellular homeostasis under metabolic stress (7). Emerging evidence indicates that autophagy serves a complex, dual role in tumor development. In a mouse model of KRAS-driven NSCLC, early inhibition of the autophagy-related gene *ATG5* was shown to activate hypoxia-inducible factor 1-α-dependent ectonucleoside triphosphate diphosphohydrolase 1 expression, which promoted extracellular ATP hydrolysis and established an immunosuppressive microenvironment (8). This inhibition notably increased the size and number of proliferative lesions and adenomas (9). By contrast, during later stages of tumorigenesis, autophagy facilitates the adenoma-to-adenocarcinoma transition (10). In $KRAS^{G12D}$ and $Braf^{V600E}$ mouse models, autophagy-related (ATG)7 deficiency caused the accumulation of dysfunctional mitochondria and disrupted cellular metabolism, thereby impairing cancer cell proliferation and driving tumor differentiation toward benign

oncocytomas (11-13). Collectively, these findings indicate that the impact of autophagy on lung cancer progression is highly context-dependent, involving both tumor microenvironmental remodeling and cell-autonomous metabolic and differentiation programs.

Malignant cells can actively remodel the TME through autophagic flux (14,15). Lung cancer stem cells have been reported to attenuate p53 activity, thereby upregulating zinc finger E-box-binding homeobox 1 (ZEB1) expression and enhancing cancer cell stemness. Furthermore, radiotherapy-induced cellular stress can trigger cancer-associated fibroblasts (CAFs) into releasing cytokines and reactive oxygen species (ROS), which concurrently heighten autophagy activity (16). In the A549 and H1975 NSCLC cell lines, TGFβ-1 has been documented to promote autophagy, thereby driving the epithelial-to-mesenchymal transition (EMT) (17). Similarly, CAFs promote NSCLC invasion and EMT through autophagy-dependent high mobility group box 1 (HMGB1) secretion and subsequent NF-κB pathway activation; blockade of autophagic flux in CAFs attenuates HMGB1 release and diminishes their capacity to modulate EMT and metastasis-associated gene expression (18). Within the NSCLC microenvironment, the TME largely biases autophagy toward pro-tumor, cytoprotective functions, such as survival, EMT and immune evasion (8). However, under specific stimuli, such as TMEM164-driven ferroptosis (19), the same autophagic machinery can be redirected toward antitumor outcomes. Therefore, context-specific targeting of the TME-autophagy axis, adjusted for specific cell types and pathological stages, represents a promising therapeutic strategy (20,21).

Xanthine oxidase (XO) and xanthine dehydrogenase (XDH) are interconvertible isoforms of the enzyme xanthine oxidoreductase (XOR). In normal mammalian cells, XOR is primarily synthesized as XDH. However, it can be converted into XO through oxidation of thiol groups or proteolytic cleavage (22,23). XOR is ubiquitously expressed across various human tissues and plasma, where it catalyzes the hydroxylation of a broad spectrum of substrates, including purines, xanthine, aromatic heterocycles and aromatic aldehydes (24). Its central metabolic role involves the sequential oxidation of hypoxanthine to xanthine and subsequently to uric acid. Whilst XDH is the predominant intracellular form, it frequently converts into XO in extracellular and circulatory environments (23). A notable functional distinction lies in their electron acceptor specificity, whereby XDH utilizes NAD^+ to produce NADH, whereas XO primarily utilizes O_2 to generate superoxide ($O_2^{\bullet-}$) and hydrogen peroxide (H_2O_2) (24-26). Whilst these ROS are essential for physiological signaling and immune defense, their overproduction has been implicated in ischemia-reperfusion injury and oncogenesis (22,27). Consequently, XOR expression and activity are pivotal for maintaining cellular redox homeostasis. Dysregulation of the XO/XDH ratio in malignant cells induces chronic oxidative stress, which may function as a stimulus for pro-tumor autophagy, as ROS activate autophagy via AMP-activated protein kinase (AMPK)-dependent mTOR suppression (28,29).

Preliminary clinical studies have demonstrated that erythrocyte XO activity is markedly elevated in patients with both NSCLC and SCLC compared with that in healthy cohorts. Specifically, in advanced NSCLC, a positive association exists between erythrocyte malondialdehyde levels and erythrocyte XO activity, suggesting that XO is associated with the systemic oxidative stress imbalance in pulmonary malignancies (30). In addition, immunohistochemical analysis of specimens from 82 patients with NSCLC previously revealed no significant association between XOR expression and patient survival. Notably, within the subset of 34 XOR-positive cases treated with adjuvant chemotherapy, lower XOR expression was associated with improved survival (31). These data suggest a potential relationship between XOR and NSCLC. However, the specific mechanism by which XOR impacts NSCLC remains to be elucidated.

Mechanistic studies have begun to elucidate the functional role of XOR in lung cancer. Wang *et al* (32) previously found that *Astragalus* polysaccharides can inhibit XO-induced autophagy in the A549 cell line. Febuxostat (FBX) is a 2-(3-cyano-4-isobutoxyphenyl)-4-methyl-1, 3-thiazole-5-carboxylic acid that has been characterized as a potent, orally active, non-purine selective XOR inhibitor. It is typically clinically indicated for the management of chronic hyperuricemia in gout (33,34). Alfaifi *et al* (35) synthesized FBX-[poly(lactic-co-glycolic acid); PLGA]-polyethylene glycol (PEG) by encapsulating FBX into PLGA nanoparticles and subsequently validated its cytotoxic efficacy in A549 LUAD cells. Despite these findings, the specific role of XOR in NSCLC and its downstream regulatory mechanisms remain incompletely elucidated.

The present study was designed to investigate the role of XOR in NSCLC progression and to evaluate the therapeutic potential of its pharmacological inhibitor, FBX. The specific aims were: i) To compare XOR expression and enzymatic activity between NSCLC cell lines and normal bronchial epithelial cells; ii) to determine the impact of small interfering RNA (siRNA)-mediated XOR knockdown on NSCLC cell viability, apoptosis, migration and invasion; iii) to assess the effects of FBX-mediated pharmacological XOR inhibition on NSCLC malignant phenotypes; and iv) to elucidate the underlying molecular mechanisms, with a particular focus on pro-survival autophagy pathways. Collectively, these investigations aimed to establish XOR as a novel metabolic target and to provide preclinical evidence supporting repurposing of FBX for NSCLC treatment.

Materials and methods

Bioinformatics and data acquisition. The Tumor Immune Estimation Resource (TIMER) database (https://cistrome.shinyapps.io/timer/) was utilized to evaluate XDH gene expression across various cancer types. The relationship between XDH expression and OS or survival until first progression (FP) in lung cancers was examined using the Kaplan-Meier (KM) Plotter (https://kmplot.com/analysis/). Hazard ratios (HRs) with 95% CIs and log-rank P-values were also calculated. The Gene Expression Profiling Interactive Analysis (GEPIA; http://gepia2.cancer-pku.cn/) is an interactive platform that provides data for 60,000 genes and 198,000 isoforms from TCGA and Genotype-Tissue Expression (GTEx) projects, focusing on RNA sequencing expression. The correlation analysis of XDH expression and autophagy gene markers in LUAD and LUSC was conducted in GEPIA 2 using TCGA

and GTEx expression data, with the Spearman method applied to calculate the correlation coefficient.

Cell lines and culture. The human LUAD cell line (A549), the LUSC cell line (SK-MES-1) and normal immortalized human lung epithelial cell type (BEAS-2B) were purchased from Procell Life Science & Technology Co., Ltd. All cell lines were authenticated and routinely tested negative for mycoplasma contamination. All cell lines were grown in DMEM/High-glucose culture medium (cat. no. C3113-0500; Shanghai VivaCell Biosciences, Ltd.) supplemented with 10% FBS (cat. no. 10270-106; Gibco; Thermo Fisher Scientific, Inc.), 0.1 mg/ml streptomycin and 100 U/ml penicillin (cat. No. C3420-0100; Shanghai VivaCell Biosciences, Ltd.) at 37˚C in an environment of 5% CO_2 and 95% humidity.

Gene silencing by siRNA. Cells plated at 60% density in 6-well plate were transfected with 200 pmol of either XOR-specific siRNA or scrambled negative control using jetPRIME (Polyplus-transfection SA) as per the manufacturer's instructions. siRNA and transfection reagent were diluted in buffer, mixed and incubated at room temperature for 10 min to form transfection complexes. The complexes were then added to cells, which were subsequently maintained at 37˚C in a humidified incubator with 5% CO_2 for 6 h, after which the transfection medium was replaced with complete growth medium. At 48 h post-transfection, samples were harvested for simultaneous protein and transcript quantification, and all other functional assays. Targeting sequences for the siRNA guide strands are as follows: siRNA-NC sense, 5'-CGUACG CGGAAUACUUCGATT-3' and antisense, 5'-UCGAAGUAU UCCGCGUACGTT-3' and siRNA-XOR-sense, 5'-UUCCAC CAUAGCAAAGGGCTT-3' and antisense, 5'-GCCCUUUGC UAUGGUGGAATT-3'.

RNA extraction and reverse transcription-quantitative PCR. Total RNA was extracted from A549 and SK-MES-1 cells using a TransZol Up Plus RNA Kit (ER501-01-V2; TransGen Biotech Co., Ltd.) according to the manufacturer's instructions. RNA concentration and purity were assessed by spectrophotometry, and samples with A260/A280 ratios between 1.8 and 2.1 were retained for downstream analysis. Genomic DNA contamination was eliminated using the gDNA removal reagent supplied in the Evo M-MLV Reverse Transcription Kit (AG11705; Hunan Accurate Bio-Medical Technology Co., Ltd.). First-strand cDNA synthesis was performed with the same kit, which contains Evo M-MLV reverse transcriptase, reverse transcription buffer, dNTPs and random hexamer primers. The reverse transcription reaction was carried out at 37˚C for 15 min, followed by enzyme inactivation at 85˚C for 5 sec. Quantitative PCR was performed using the SYBR Green Premix Pro Taq HS qPCR Kit (ROX Plus) (AG11718; Hunan Accurate Bio-Medical Technology Co., Ltd.) and a QuantStudio 5 system (Applied Biosystems; Thermo Fisher Scientific, Inc.). Each 20-μl reaction mixture contained 10 μl SYBR Green master mix (containing SYBR Green I fluorophore, hot-start Taq DNA polymerase, dNTPs and optimized reaction buffer), 0.4 μM each of forward and reverse primers, and 0.2 μl diluted cDNA template. The thermocycling conditions were as follows: Initial denaturation at 95˚C for 30 sec, followed by 40 cycles of 95˚C for 5 sec and 60˚C for 30 sec. Melting curve analysis was conducted to verify primer specificity. Relative gene expression was calculated using the $2^{-\Delta\Delta Cq}$ method, as described by Livak and Schmittgen (36). The following primer pairs were used for quantitative PCR: β-actin forward, 5'-GCCGACAGGATGCAGAAGGAGA-3' and reverse, 5'-CACACGGAGTACTTGCGCTCAG-3'; and XOR forward, 5'-GCTCTGAAAATCCCCACCTC-3' and reverse, 5'-GGAGCCACTGGGATTCTTCTT-3'.

Pharmacological treatments. Cells (A549 and SK-MES-1) were pre-treated with 50 μM FBX (cat. no. SF1114; Beyotime Institute of Biotechnology), 100 nM Rapamycin (Rapa; cat. no. HY-10219; MedChemExpress), 2 nM Bafilomycin A1 (BafA1; cat. no. HY-100558; MedChemExpress) or 8 mM 3-Methyladenine (3-MA; cat. no. S2767; Selleck Chemicals) for 12 h at 37˚C in a humidified incubator with 5% CO_2 before being exposed to starvation medium (FBS-free DMEM medium) (37). A concentration of 1 mM N-Acetylcysteine (NAC; cat. no. HY-B0215; MedChemExpress) was used to scavenge ROS *in vitro* for 4 h at 37˚C in a humidified incubator with 5% CO_2. An equal volume of dimethyl sulfoxide served as the vehicle control.

ELISA. To assess XOR activity in NSCLC cells, the XO ELISA kit (cat. no. A002-1-1; Nanjing Jiancheng Bioengineering Institute) was used according to the manufacturer's instructions. The assay principle is as follows: XOR catalyzes the oxidation of hypoxanthine to xanthine, concomitantly generating superoxide anion radicals. In the presence of an electron acceptor and chromogenic reagent, a purple-red complex is formed, where XOR activity is quantified based on the intensity of this complex. Briefly, the detached cells (cells were seeded at equivalent densities and allowed to adhere overnight) were added to the reagents 1 to 4 and incubated at 37˚C for 20 min. After the addition of reagent 5, the sample's absorbance was measured at 530 nm using a 96-well plate reader.

Cell counting kit-8 (CCK-8) assay. The CCK-8 assay was performed using the CCK-8 kit (cat. no. HY-K0301; MedChemExpress) following the manufacturer's instructions. A549 and SK-MES-1 cells (1,000 cells per well) were seeded in 96-well culture plates. Subsequently, all cells were treated under starvation conditions. After 24, 48 and 72 h of incubation at 37˚C in a humidified incubator with 5% CO_2, 100 μl CCK-8 solution was added to each well. The CCK-8 solution was then incubated with the cells for an additional hour at 37˚C in a humidified incubator with 5% CO_2. A spectrophotometer was used to measure the optical density at a wavelength of 450 nm. The experiments were conducted in triplicate for biological repeats.

Flow cytometry analysis. Following the instructions of the Annexin V-mCherry/SYTOX Green cell apoptosis detection kit (cat. no. C1070S; Beyotime Biotechnology), cells were treated with FBX for 36 h at 37˚C in a humidified incubator with 5% CO_2. After treatment, the cells were washed with PBS and centrifuged. The binding buffer was then added and the samples were centrifuged again before being washed. Subsequently, the samples were stained at room temperature

for 30 min with Annexin V-mCherry and SYTOX Green. The analysis of the samples was performed using the BD FACSCantoTM II system (BD Biosciences), and the data were analyzed with FlowJo software (version 10.8.1; BD Biosciences).

Colony formation assay. A549 and SK-MES-1 cells were seeded in a 6-well plate at a density of 400 cells per well and incubated with FBX in starvation medium for 15 days at 37˚C in a humidified incubator with 5% CO_2. Afterward, the colonies were treated with 0.1% crystal violet at room temperature for 15 min, before the stained areas were analyzed using ImageJ software (version 1.8.0; National Institutes of Health).

Scratch cell migration assay. A549 and SK-MES-1 cells were cultured in complete medium supplemented with 10% FBS in 6-well plates until they reached 90% confluency. Following a 12-h pre-treatment with FBX at 37˚C in a humidified incubator with 5% CO_2, the cell monolayer was disrupted using the tip of a sterile 100-μl pipette. Detached cells were removed by washing with PBS, and the medium was subsequently replaced with serum-free medium. Following scratching, cells were maintained at 37˚C in a humidified incubator with 5% CO_2. The wound area was imaged using an Mshot light microscope camera (Guangzhou Mingmei Optoelectronic Technology Co., Ltd.). The distance of the wound gap was measured and calculated using ImageJ software (version 1.8.0). The migration rate was determined using the formula migration rate=[(initial gap at 0 h-final gap at 24 or 48 h)/initial gap at 0 h] x100%. The experiment was conducted three times and the results are presented as mean ± SEM.

Transwell cell invasion assay. A549 and SK-MES-1 cells were treated with or without FBX for 10 h at 37˚C in a humidified incubator with 5% CO_2 and then plated into 24-well Transwell inserts (8-μm pore size; cat. no. 3422; Corning, Inc.). The upper chamber was coated with 80 μl (1 mg/ml) Matrigel matrix (cat. no. 356234; Corning, Inc.) in serum-free medium for 30 min at 37˚C in a humidified incubator with 5% CO_2. Subsequently, NSCLC cells suspended in serum-free DMEM were seeded into the upper chamber at a density of 60,000 cells per well. Each well of the 24-well plates contained 500 μl DMEM with 20% FBS. After 15 h of incubation at 37˚C in a humidified incubator with 5% CO_2, the cells that migrated to the lower face of the inserts were fixed with 4% paraformaldehyde at room temperature for 10 min. The migrated cells at the bottom of the upper chamber were stained with 0.1% crystal violet (cat. no. E607309; Sangon Biotech Co., Ltd.) at room temperature for 2 h and imaged under a light microscope at 100x magnification in 10 randomly chosen fields. The number of migrated cells was quantified using ImageJ software (version 1.8.0; National Institutes of Health).

Western immunoblot analysis. Proteins for western blotting were extracted using RIPA lysis buffer (cat. no. 9806; CST Biological Reagents Co., Ltd.) with a Protease/Phosphatase Inhibitor Cocktail (cat. no. 5871s; CST Biological Reagents Co., Ltd.). Immunoblotting analysis was conducted using the Bio-Rad Bis-Tris Gel system (Bio-Rad Laboratories, Inc.) following the manufacturer's guidelines. Protein concentrations were determined using a BCA protein assay kit (cat. no. G2026-200T; Wuhan Servicebio Technology Co., Ltd.) according to the manufacturer's instructions, and equal amounts of protein (20 μg per lane) were loaded onto a Bio-Rad Bis-Tris Gel (Bio-Rad Laboratories, Inc.). Primary antibodies were utilized to detect the following proteins: Phosphorylated (p-)-mTOR (1:1,000; cat. no. HA1224; GenXspan, Inc.), mTOR (1:1,000; cat. no. HL0418; GenXspan, Inc.), XDH (1:1,000; cat. no. 55156-1-AP; Proteintech Group, Inc.), Fibronectin (1:1,000; cat. no. 66042-1-lg; Proteintech Group, Inc.), N-cadherin (1:1,000; cat. no. 22018-1-AP; Proteintech Group, Inc.), E-cadherin (1:1,000; cat. no. 20874-1-AP; Proteintech Group, Inc.), p62/SQSTM1 (1:1,000; cat. no. 66184-1-Ig; Proteintech Group, Inc.), LC3 (1:1,000; cat. no. 14600-1-AP; Proteintech Group, Inc.) and GAPDH (1:3,000; cat. no. 60004-1-Ig; Proteintech Group, Inc.). Proteins were separated on a 7.5% SDS-PAGE gel and transferred onto a PVDF membrane by electrophoresis. The membrane was subsequently blocked with 5% non-fat dry milk (Sangon Biotech Co., Ltd.) in TBS with 0.1% Tween-20 at room temperature for 1 h. The proteins were incubated with antibodies for 12 h at 4˚C, followed by a 2-h incubation at room temperature with an HRP-conjugated secondary antibody (1:5,000; cat. nos. SA00001-1 and SA00001-2; Proteintech Group, Inc.). Detection was performed using Pierce ECL Western Blotting Substrate (Thermo Fisher Scientific, Inc.) and visualized on an iBright CL1000 imaging system (Thermo Fisher Scientific, Inc.). Protein bands were semi-quantified using ImageJ (version 1.8.0; National Institutes of Health).

Fluorescent analysis of acidic lysosome. Cells that reached 90% confluence were placed in starvation medium (previously treated with FBX for 2 h) for durations of 4 and 8 h at 37˚C in a humidified incubator with 5% CO_2. Following this, the cells were stained with 50 nM Lyso-Tracker Red at 37˚C for 30 min. The resulting red fluorescence intensities were immediately observed using a fluorescence microscope (Axio Vert. A1; Zeiss AG) at 400X magnification with consistent exposure time. The fluorescent areas were analyzed using ImageJ software (version 1.8.0; National Institutes of Health).

Quantitative measurement of free radical production. The production of intracellular ROS was assessed according to the manufacturer's instructions (cat. no. S0033S; Reactive Oxygen Species Assay Kit; Beyotime Institute of Biotechnology). Briefly, intracellular ROS levels were evaluated using DCFH-DA. The cells were cultured in 96-well plates, where after treatment, they were exposed to 10 μM DCFH-DA at 37˚C in a CO_2 incubator for 30 min, followed by two washes with 200 μl serum-free DMEM medium. The fluorescent intensities were then quantified immediately using a fluorescent microplate reader (Synergy H1 multi-mode plate reader, BioTek Instruments; Agilent Technologies, Inc.) with an excitation wavelength of 488 nm and an emission wavelength of 525 nm.

Statistical analysis. Every experiment was conducted three times under identical conditions. Data are presented as means with standard error of the mean and were statistically evaluated using GraphPad Prism software version 7.01 (Dotmatics). Unpaired Student's t-test was employed to compare the test

and control sample values and one-way ANOVA with Tukey's multiple comparisons test were used for multiple groups comparisons. P<0.05 was considered to indicate a statistically significant difference.

Results

XOR is overexpressed in NSCLC and targetable by febuxostat. XO is generated from its precursor XDH by reversible thiol oxidation or irreversible proteolytic cleavage. Therefore, XDH expression levels serve as a reliable surrogate indicator of total XOR capacity (23). To evaluate the clinical and biological relevance of this pathway in NSCLC, XOR expression was characterized in lung adenocarcinoma (A549), squamous cell carcinoma (SK-MES-1) and relative to normal lung epithelial cells line BEAS-2B. Western blot analysis demonstrated that XOR had significantly greater expression in both A549 and SK-MES-1 cells compared with that in BEAS-2B cells (Fig. 1A). Similarly, the present analysis of the TIMER public database confirmed that XDH expression is markedly elevated in primary LUAD and LUSC tissues compared with that in adjacent normal tissues (Fig. 1B). Furthermore, ELISA showed that XOR activity was significantly higher in both NSCLC cell lines compared with that in BEAS-2B cells (Fig. 1C).

To evaluate the prognostic significance of XOR in lung cancer, the association between XDH expression and both OS and survival until FP was analyzed using the KM Plotter database (Fig. 1D). High XDH expression was significantly associated with diminished OS (HR=1.24; 95% CI, 1.07-1.43) and markedly reduced FP survival (HR=2.01; 95% CI: 1.63-2.48). Collectively, these clinical data indicate that elevated XOR is a negative prognostic indicator, suggesting that XOR activity contributes to disease progression and an increased risk of tumor recurrence following initial therapy, consistent with previous reports (38-40).

To validate the role of XOR in NSCLC, XOR expression was knocked down in NSCLC cell lines using siRNA. Significant depletion of XOR was achieved at both protein and mRNA expression levels in A549 and SK-MES-1 cells (Figs. 1E and S1A). XOR knockdown was found to significantly reduce cell viability (Fig. 1F). Furthermore, wound healing and Matrigel-Transwell invasion assays demonstrated impaired migratory and invasive capacity upon XOR silencing (Fig. 1G and H).

As a Food and Drug Administration-approved XOR inhibitor (41), the effects and mechanisms of FBX in NSCLC were next investigated. In the preliminary experiments of the present study, even at concentrations up to 200 μM (data not shown), FBX failed to achieve complete cell killing under nutrient-deprived conditions, where A549 cells maintained ~40% viability, whilst in SK-MES-1 cells, 200 μM FBX showed an even weaker response (~50% viability). Therefore, 50 μM was adopted as the minimum concentration affecting cell viability for subsequent experiments. ELISA revealed that 50 μM FBX significantly reduced XOR enzymatic activity in both A549 and SK-MES-1 cells (Fig. 2A), accompanied by a significant decrease in cell viability under starvation conditions (Fig. 2B), suggesting that XOR inhibition effectively impairs NSCLC cell proliferation. Clonogenic assays demonstrated that FBX significantly compromised long-term cell survival, evidenced by a substantial reduction in colony coverage area compared with that in the control group after 15 days (Fig. 2C). Flow cytometric analysis revealed that FBX significantly increased the proportion of early apoptotic cells without markedly affecting the proportion of late apoptotic cells in both A549 and SK-MES-1 cell lines (Fig. 2D). The selective accumulation of early apoptotic cells may be attributed to the moderate metabolic stress induced by serum deprivation. Unlike complete nutrient starvation, the absence of serum alone may be insufficient to propel cells through the full apoptotic cascade into late apoptotic or secondary necrotic stages, thereby resulting in a predominant early apoptotic phenotype (42). Consistent with the siRNA knockdown results, Matrigel-transwell assays confirmed that FBX significantly reduced the invasive potential of NSCLC cells (Fig. 2E). Scratch wound-healing assays showed that FBX treatment significantly attenuated the migratory capacity of both cell types (Fig. 2F). Collectively, these findings established that FBX can exert potent antitumor effects by inhibiting proliferation, inducing apoptosis and suppressing the migratory/invasive hallmarks of NSCLC.

To explore the potential mechanisms underlying FBX-induced phenotypic changes in NSCLC cells, intracellular ROS levels were examined. In A549 cells, FBX treatment elicited a significant increase in ROS within 30 min, irrespective of whether cells were maintained under standard culture conditions or nutrient-deprived conditions (Fig. S2A). Notably, under starvation conditions, this ROS elevation was substantially attenuated by pretreatment with NAC for 4 h (Fig. S2B). Concordantly, NAC significantly counteracted FBX-induced cytotoxicity in both A549 and SK-MES-1 cells (Fig. S2C). These data indicate that FBX can disrupt cellular redox homeostasis by XOR blockade, subsequently driving ROS-mediated proliferation inhibition.

Effect of FBX on NSCLC cells is associated with autophagy. Previous studies have established that FBX-mediated XOR inhibition can induce intracellular ROS accumulation, a process intricately associated with the regulation of autophagy (37,43). In the present study, FBX had minimal impact on NSCLC cell viability under standard culture conditions (Fig. S1B), yet markedly suppressed cell viability under nutrient-deprived conditions (Fig. 2B), a condition known to induce cytoprotective autophagy. Consequently, we hypothesized that FBX modulate NSCLC phenotypes by suppressing autophagic activity. To explore the clinical relevance of this association, the correlation between XOR expression and key autophagy-related markers was analyzed using the GEPIA2 database (integrating TCGA and GTEx datasets). The analysis revealed that XOR expression positively correlated with several essential autophagy regulators, including Beclin-1 (BECN1, R=0.18), autophagy cargo receptor (R=0.19), ATG7 (R=0.22), ATG10 (R=0.13), ATG12 (R=0.19), ATG13 (R=0.13), ATG14 (R=0.22), autophagy and beclin 1 regulator 1 (R=0.21) and lysosomal-associated membrane protein 2 (LAMP2; R=0.18; Fig. 3A). These data reveal weak but statistically significant correlations between XOR signaling and pro-survival autophagy markers in NSCLC. Whilst these associations are consistent with a potential role in tumor maintenance and immune evasion, further functional studies are warranted to establish causal relationships.

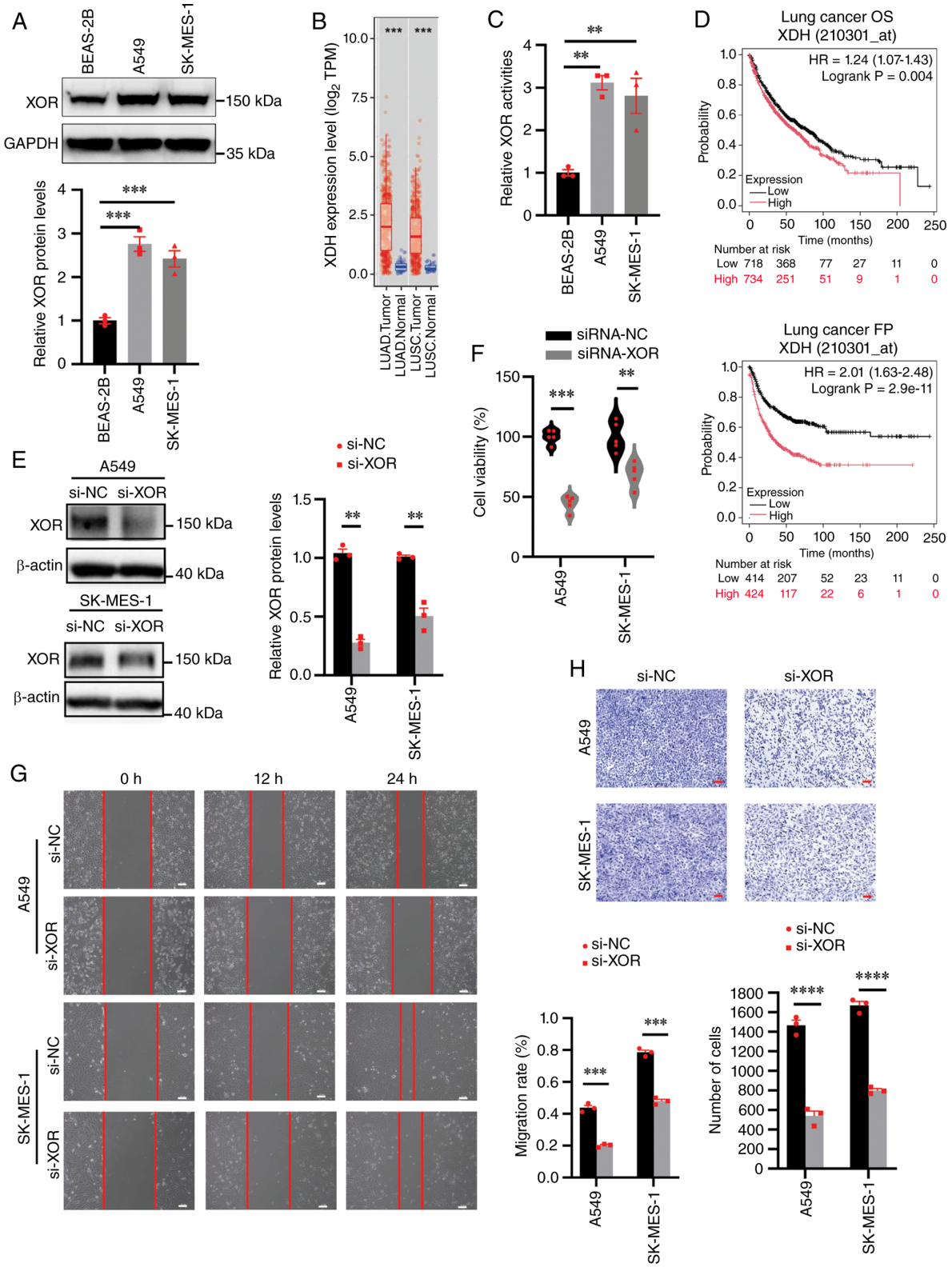


Figure 1. XOR level positively associated with NSCLC. (A) Expression of XOR is increased in NSCLC cells compared with that in normal cells. (B) XDH expression levels in lung cancers from The Cancer Genome Atlas database were determined by the TIMER database. (C) Activity of XOR is increased in NSCLC cells compared with that in normal cells. (D) Kaplan-Meier analysis of survival according to XDH expression status in patients with lung cancer using Kaplan-Meier plotter. High XDH expression was associated with worse OS and survival until FP in lung cancer cohorts (n=1,452 and n=838, respectively). (E) XOR protein levels in A549 and SK-MES-1 cells after 48 h siRNA-transfection. (F) Cell counting kit-8 cell proliferation assay evaluating the viability of A549 and SK-MES-1 cells transfected with siRNA-NC or siRNA-XOR after 72 h. (G) Cell migration was analyzed by the scratch assay. A549 and SK-MES-1 cells transfected with siRNA-NC or siRNA-XOR were seeded in 6-well plates and wounded by a 100 μl pipette tip. The cells were then imaged at 12-h intervals for recording migration. Scale bar, 20 μm. (H) A549 and SK-MES-1 cells transfected with siRNA-NC or siRNA-XOR were seeded in a chamber covered with a diluted Matrigel matrix. The invading cells were stained and observed at x20 magnification after 12 h. Scale bar, 20 μm. All the values represent the mean ± SEM of three independent experiments. ****P≤0.0001, ***P≤0.001 and **P≤0.01. XOR, xanthine oxidoreductase; NSCLC, non-small cell lung cancer; LUAD, lung adenocarcinoma; LUSC, lung squamous cell carcinoma; XDH, xanthine dehydrogenase; OS, overall survival; FP, first progression; siRNA or si, small interfering RNA; NC, negative control; HR, hazard ratio.

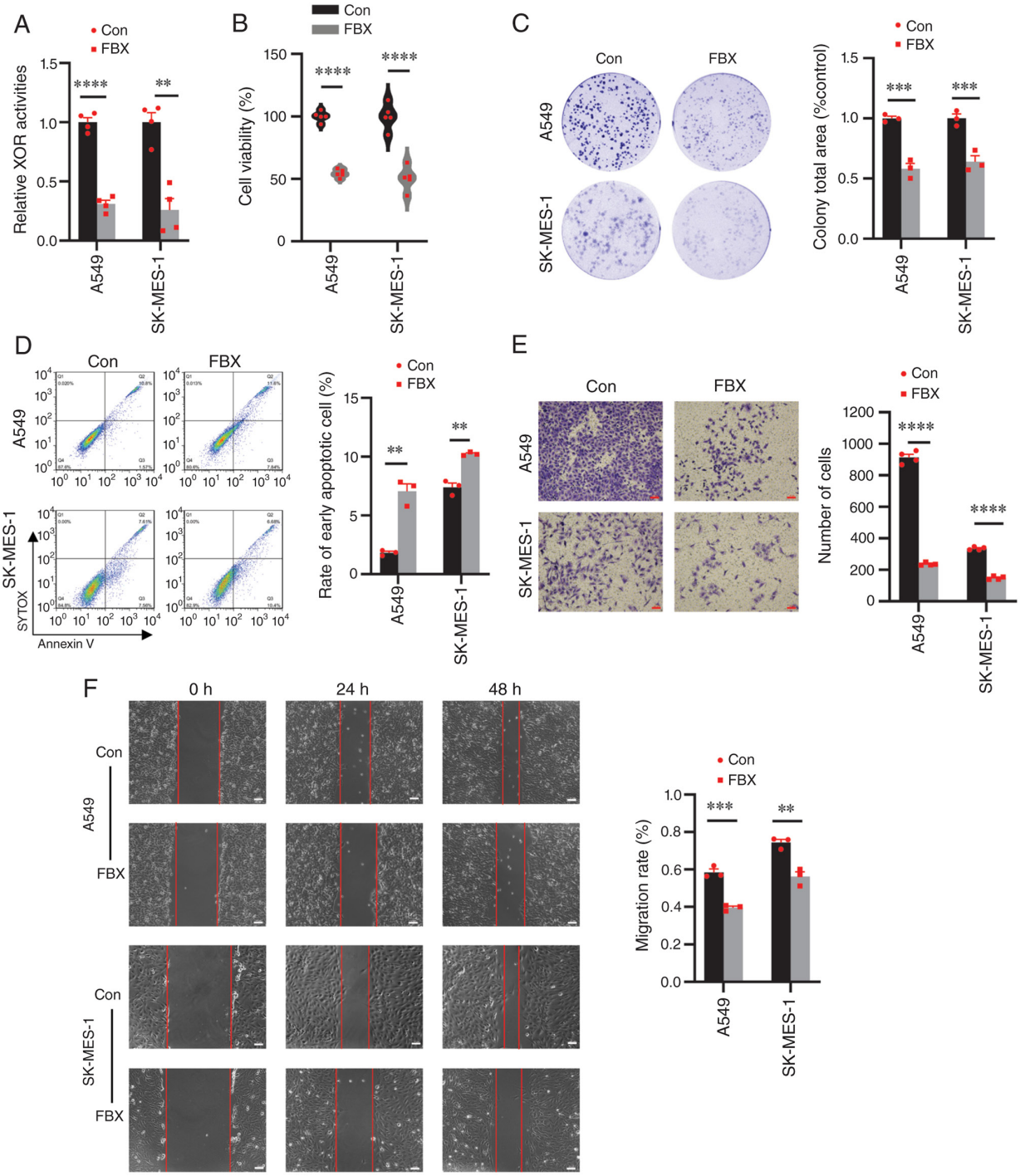


Figure 2. FBX prevents non-small cell lung cancer cells from colony formation, migration, and invasion whilst promoting apoptosis under serum starvation conditions. (A) The XOR activities of A549 and SK-MES-1 cells pre-treated with FBX or DMSO were analyzed by ELISA. The data are presented as the mean ± SEM of four separate experiments. (B) Cell counting kit-8 cell proliferation assay evaluating the viability of A549 and SK-MES-1 cells pre-treated with FBX or not after 72 h. The data are presented as the mean ± SEM of five separate experiments. (C) Colony formation assay of A549 and SK-MES-1 cells treated with FBX. Colonies were counted after 15 days. The data are presented as the mean ± SEM of three separate experiments. (D) Flow cytometry determined A549 and SK-MES-1 apoptosis after 48 h of starvation. FBX treatment was performed for 12 h before starvation. The data are presented as the mean ± SEM of three separate experiments. (E) A549 and SK-MES-1 cells treated with FBX were seeded into a chamber covered with a diluted Matrigel matrix. The invading cells were stained and observed at x20 magnification after 15 h. Quantitative analysis of numbers of invading cells. Scale bar, 20 μm. The data are presented as the mean ± SEM of four separate experiments. (F) Cell migration was analyzed by the scratch assay. A549 and SK-MES-1 cells treated with FBX were seeded in 6-well plates and wounded by a 100-μl pipette tip. The cells were then imaged at 24-h intervals for recording migration. Cell migration rate was measured and calculated. Scale bar, 20 μm. The data are presented as the mean ± SEM of three separate experiments. ****P≤0.0001, ***P≤0.001 and **P≤0.01. FBX, febuxostat, XOR, xanthine oxidoreductase; Con, control.

To validate the relationships of autophagy and XOR, 3-MA, a class III PI3K inhibitor that blocks autophagosome formation, was applied (44). Consistent with the effects of FBX, 3-MA treatment significantly reduced cell viability and migratory capacity in both A549 and SK-MES-1 cells (Fig. 3B and C).

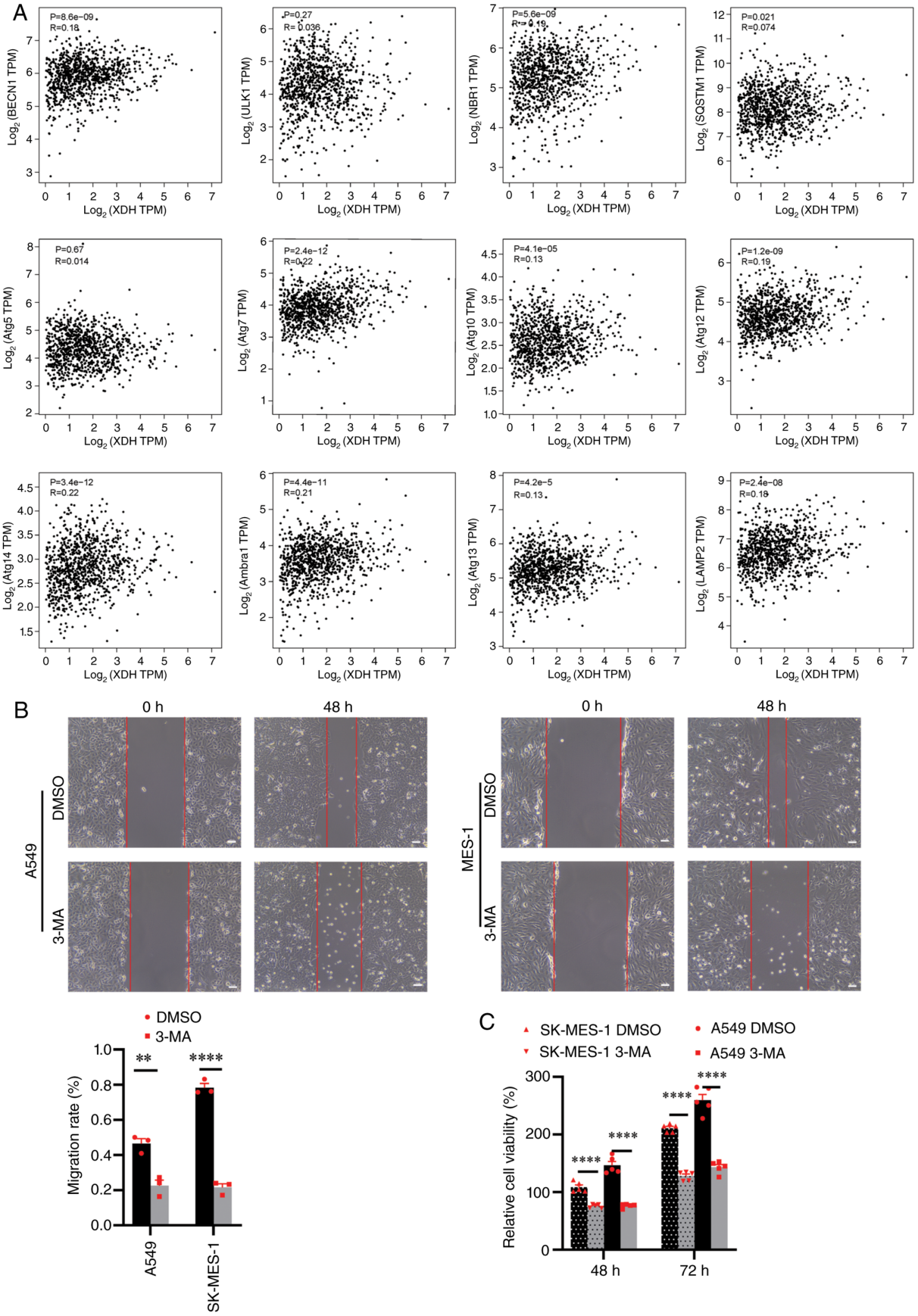


Figure 3. Relationship between XOR expression levels and autophagy-related protein markers in NSCLC tissues. (A) Analysis of the correlation between XOR expression and autophagy marker expression levels in NSCLC tissue using the GEPIA2 database. (B) Cell migration was analyzed by scratch assay. A549 and SK-MES-1 cells treated with 3-MA were seeded in 6-well plates and wounded by a 100-μl pipette tip. The cells were then grown for 48 h for imaging. Scale bar, 20 μm. The data are presented as the mean ± SEM of three separate experiments. (C) 3-MA affected the proliferation of NSCLC cells. The data are presented as the mean ± SEM of five separate experiments. ****P≤0.0001 and **P≤0.01. XOR, xanthine oxidoreductase; NSCLC, non-small cell lung cancer; 3-MA, 3-methyladenine; XDH, xanthine dehydrogenase; TPM, transcripts per million.

Since the formation of acidic autolysosomes is a hallmark of late-stage autophagy flux, the acidophilic probe Lyso-Tracker Red was utilized to monitor lysosomal fusion. Following FBX treatment under starvation conditions, A549 cells exhibited a significant reduction in red puncta and fluorescence intensity at 4 and 8 h compared with controls (Fig. 4A and B), indicating an impairment of autophagic flux.

Furthermore, the FBX-induced reduction in autophagosome formation was fully rescued by Rapa, a specific mTOR inhibitor and autophagy activator (Fig. 4C and D). Notably, cell proliferation assays demonstrated that the anti-proliferative effect of FBX on A549 and SK-MES-1 cells was significantly attenuated by Rapa-mediated autophagy induction (Fig. 4E and F). Collectively, these findings suggest that the anti-tumor efficacy of FBX is mechanistically driven by the suppression of the autophagic pathway.

FBX elicits changes in the expression of autophagy signaling pathway components. To further elucidate the regulatory effect of FBX on autophagy, the expression of key autophagic proteins in A549 cells under starvation-induced stress was next assessed (Fig. 5A). The lipidation of LC3-I to LC3-II serves as a key indicator of early autophagosome formation, whereas p62/SQSTM1 acts as a selective autophagy receptor that is degraded during functional autophagic flux (45). In control cells, LC3-II levels initially decreased upon starvation but subsequently stabilized, suggesting a continuous state of autophagosomes biogenesis. By contrast, p62 expression increased immediately following starvation and began to decline after 4 h, reflecting progressive autophagic degradation in alignment with established starvation-response models (46,47). Compared with the DMSO control, FBX treatment under nutrient-deprived conditions for 4 h resulted in a more pronounced decrease in LC3-II expression. Although p62 levels also declined in the FBX group, the reduction was markedly slower than that in the DMSO group, leading to greater p62 accumulation. This simultaneous reduction in LC3 lipidation and accumulation of p62 indicates that FBX impaired both autophagosome biogenesis and lysosomal clearance capacity (Fig. S3D and E). Furthermore, a significant reduction in Beclin-1 expression confirmed that FBX could disrupt the initiation of starvation-induced autophagy (Fig. S3A). Parallel to these autophagic changes, FBX treatment downregulated the mesenchymal markers fibronectin (Figs. 5A and S3A) and N-cadherin (Fig. 5B), while upregulating the epithelial marker E-cadherin (Figs. 5A and B, and S3A). These reciprocal alterations in EMT-associated proteins indicated that FBX inhibited the mesenchymal phenotypes of NSCLC cells. These observations were corroborated by 3-MA treatment, which similarly induced LC3-II depletion and p62 accumulation whilst eliciting alterations in fibronectin protein levels (Figs. 5C, and S3B and C).

To further validate FBX-mediated autophagy inhibition in NSCLC, cells were co-treated with BafA1 for 24 h in starvation medium. BafA1 alone caused accumulation of p62 and LC3-II in both A549 and SK-MES-1 cells, confirming blockade of autophagosome-lysosomal degradation. Notably, FBX differentially affected autophagic flux between the two cell lines (Fig. 5B). In SK-MES-1 cells, FBX induced p62 and LC3-II accumulation comparable to BafA1. However, combined treatment did not further increase these levels, indicating near-maximal autophagy inhibition by BafA1. In A549 cells, FBX elevated p62 without altering LC3-II, whereas BafA1 co-treatment likewise failed to trigger additional LC3-II accumulation, suggesting diminished autophagic flux. Collectively, these results demonstrate that FBX can inhibit autophagy in NSCLC cells.

Based on a prior finding that the autophagy inducer Rapa can reverse FBX-induced cytotoxicity in NSCLC cell lines (Fig. 4E and F), it was then hypothesized that FBX-mediated antitumor effects are autophagy-dependent. To assess this, A549 cells were subjected to starvation and treated with FBX (Fig. 6A; lane 8), Rapa (Fig. 6A; lane 9) or a combination of FBX and Rapa (Fig. 6A; lane 10). Under nutrient-deprived conditions, compared with the DMSO control (Fig. 6A; lane 6), FBX treatment induced p62 accumulation (Fig. S3F) and reduced the LC3-II/LC3-I ratio (Fig. S3G), with effects similar to those observed following 3-MA treatment (Fig. 6A; lane 7). Notably, the autophagy-inhibiting effect of FBX was attenuated by Rapa-mediated autophagy induction (Fig. 6A; lane 10), as evidenced by a restoration of the LC3-II/LC3-I ratio and a substantial decrease in p62 expression (Fig. S3F and G). However, these alterations were not observed under standard culture conditions (Fig. 6A; lanes 1-5). Similarly, under nutrient-deprived conditions, FBX treatment increased p62 accumulation in SK-MES-1 cells without markedly affecting LC3-II conversion (Figs. 6B and S3H), consistent with the aforementioned observations (Fig. 5B). Furthermore, rapamycin partially alleviated FBX-induced p62 buildup (Fig. 6B; lane 8), further supporting an autophagy-dependent mechanism. By contrast, under standard culture conditions with sufficient nutrients, FBX exerted minimal effects on LC3-II conversion and p62 turnover (Fig. 6B; lane 2), consistent with the low basal autophagic flux observed in non-starved NSCLC cells. Collectively, these results demonstrate that FBX acts as a potent inhibitor of the autophagic pathway, where its phenotypic effects can be partially rescued by pharmacological autophagy activation.

Discussion

In the present study, it was demonstrated that XOR knockdown significantly impaired the proliferation and invasive/migratory potential of NSCLC cells. This follows our initial observation of elevated XOR levels in both NSCLC cell lines and clinical tissue specimens in the present study. FBX markedly reduced XOR activity and proliferation in NSCLC cells under nutrient-deprived conditions. Furthermore, FBX treatment significantly attenuated the migratory and invasive capacities of NSCLC cells *in vitro*. Mechanistically, the anti-tumor efficacy of FBX appears to be mediated through the suppression of the autophagy signaling pathway. Notably, the induction of autophagy through pharmacological activators abrogated the tumor-suppressive effects of FBX. Beyond its primary role in reducing serum urate levels, FBX has been proposed as a protective agent against acute renal failure and tumor lysis syndrome (48). The clinical utility of FBX in oncological care is supported by both hepatoma rodent models and malignant tumor multicenter clinical investigations (49,50). These data suggest that FBX, an established gout therapeutic, may warrant

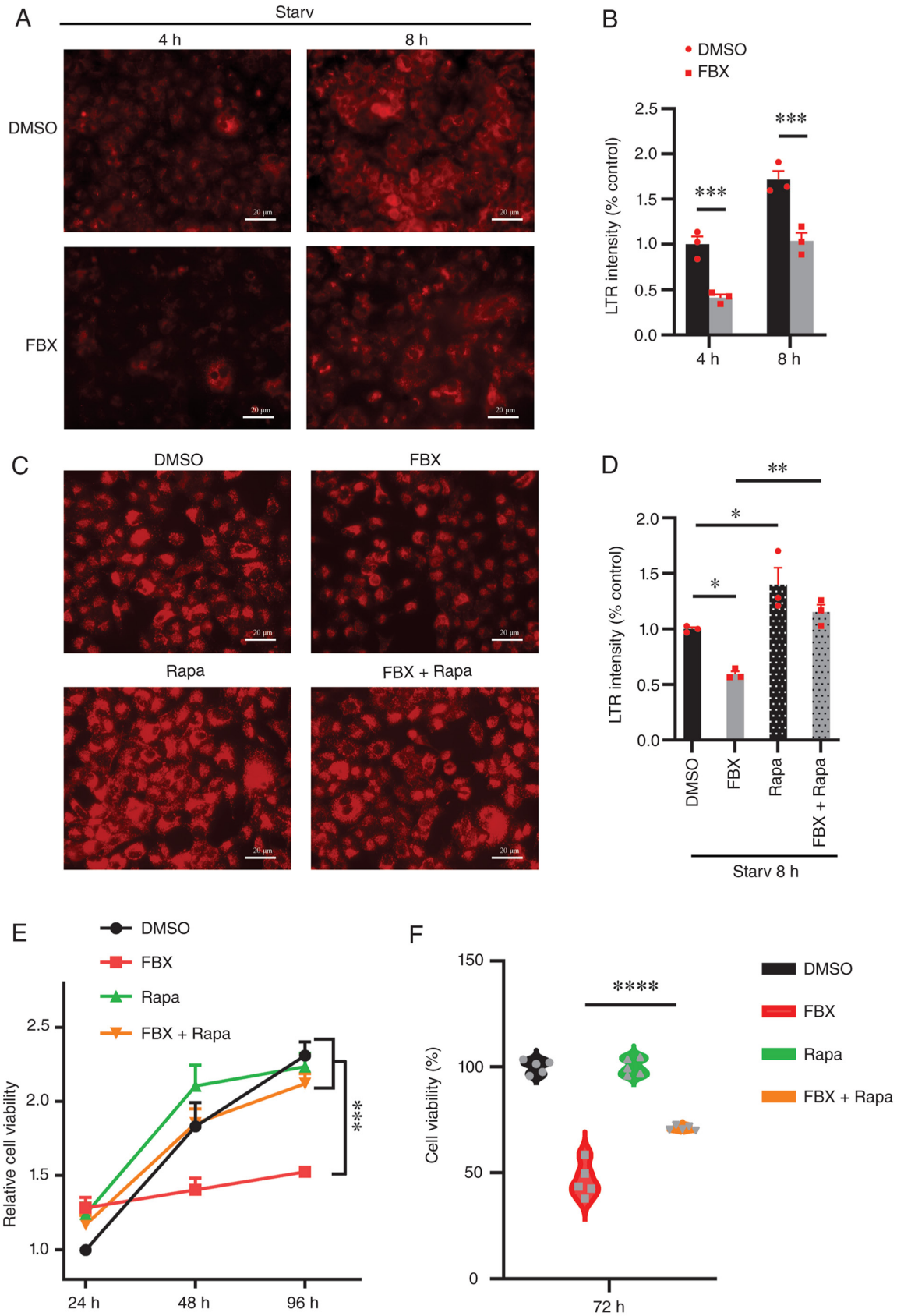


Figure 4. Effect of FBX on non-small cell lung cancer cells is associated with autophagy. (A) Assessment of autolysosome formation in A549 pre-treated with FBX after starvation at 4 and 8 h. Scale bar, 20 μm. (B) The relative LTR fluorescent activity was quantified through ImageJ software. The data are presented as the mean ± SEM of three separate experiments. (C) Lysosomal activation and repression were analyzed using the acidophilic probe LTR. A549 cells were pre-treated with FBX, Rapa and FBX + Rapa after starvation at 8 h. Lysosomes/autolysosomes were labeled with LTR and then subjected to fluorescent microscopy analysis. Scale bar, 20 μm. (D) The relative LTR fluorescent activity was quantified through ImageJ software. The data are presented as the mean ± SEM of three separate experiments. Cell counting kit-8 cell proliferation assay evaluating the viability of A549 and SK-MES-1 cells pre-treated with FBX, Rapa and FBX + Rapa at (E) 24, 48 and 96 h, and (F) 72 h. The data are presented as the mean ± SEM of five separate experiments. ****P≤0.0001, ***P≤0.001, **P≤0.01 and *P<0.05. FBX, febuxostat; Rapa, rapamycin; LTR, Lyso-Tracker Red; Starv, starvation.

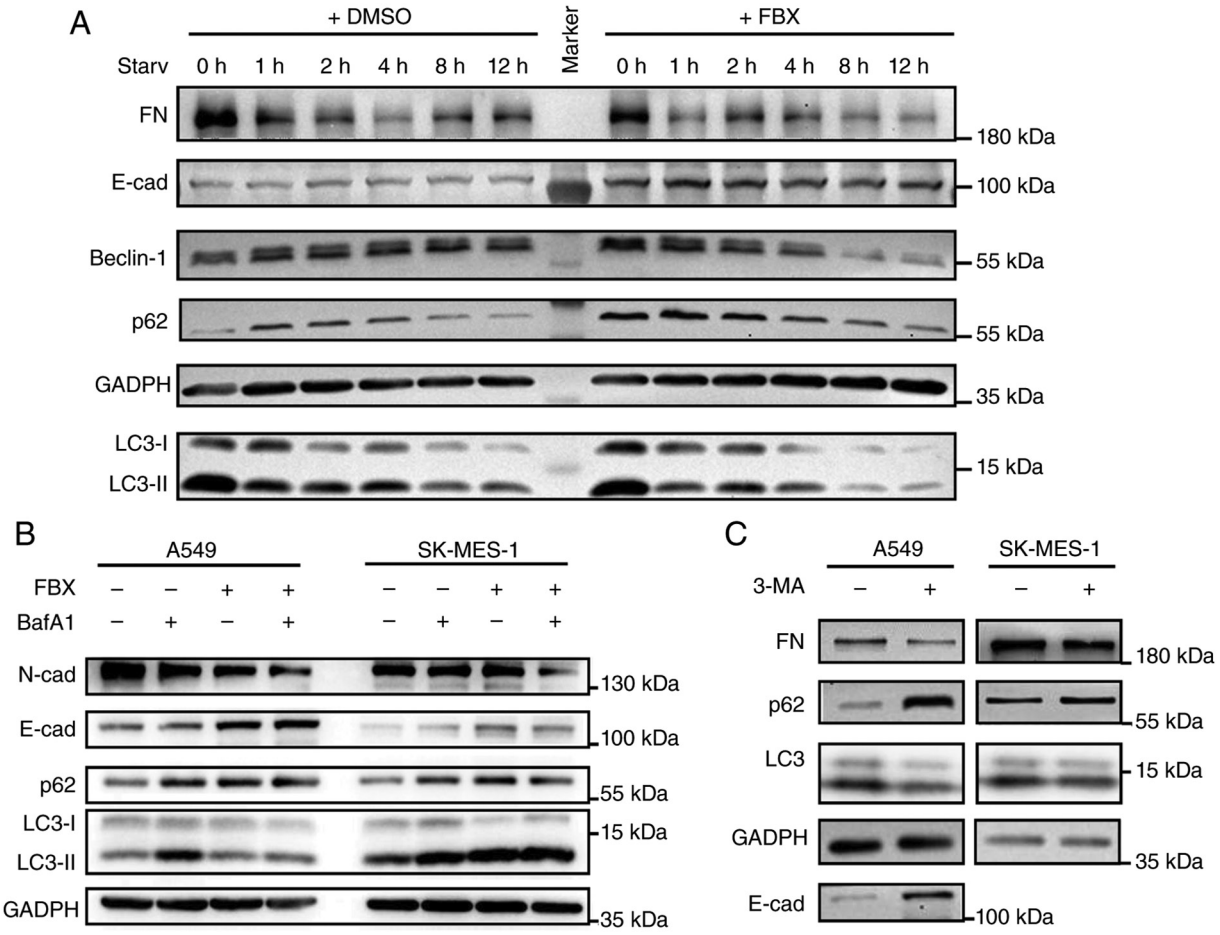


Figure 5. FBX changed the gene expression of autophagy signaling pathways in non-small cell lung cancer. (A) The expression levels of FN, E-cadherin, Beclin-1, p62 and LC3 proteins in A549 cells treated with FBX were analyzed by western blotting. (B) The expression levels of N-cad, E-cad, p62 and LC3 proteins in A549 and SK-MES-1 cells treated with FBX and/or BafA1 for 24 h in starvation medium were analyzed by western blotting. (C) The expression levels of FN, E-cad, p62 and LC3 proteins in A549 and SK-MES-1 cells treated with 3-MA were analyzed by western blotting. FN, fibronectin; Cad, cadherin; BafA1, bafilomycin A1; FBX, febuxostat; 3-MA, 3-methyladenine.

further preclinical investigation for potential repurposing in malignant tumors, with a therapeutic profile that could prove comparable or superior to the purine-analog inhibitor allopurinol.

KM Plotter database analysis revealed that elevated XOR expression is associated with shorter OS and shorter time to FP survival in patients with NSCLC. However, this finding appears inconsistent with a prior clinical study reporting reduced survival in chemotherapy-treated patients with low XOR expression, as determined by immunohistochemistry (IHC) of tumor tissues (31). These differences could be explained by the different methodological approaches. First, the IHC-based approach classified all unstained slides as XOR-negative (29/82 cases, 35%), whereas KM Plotter database mainly leveraged on microarray sequencing data, which would likely categorize these samples as low-expression rather than absent, potentially yielding different outcomes. In addition, this previous study (31) utilized a selected subset. Amongst the 53 IHC-positive cases, only 34 received adjuvant chemotherapy and the final comparison only involved 14 low-vs. 20 high-expression samples. By contrast, the KM Plotter database is comprised of >700 cases for OS and 400 cases for FP, utilizing sequencing data with superior accuracy and statistical power. Finally, the present experiments demonstrated significantly elevated XOR activity in NSCLC cell lines compared with that in normal lung epithelial cells. Both siRNA-mediated knockdown and pharmacological inhibition of XOR by FBX exerted anti-tumor effects, supporting an oncogenic role for XOR in NSCLC progression.

The anti-tumor properties of FBX were first characterized by Oh *et al* (51), who demonstrated that FBX can reduce ROS production and MAPK phosphorylation, thereby inhibiting metastasis in a murine model of hyperlipidemic breast cancer. A subsequent study showed that the encapsulation of FBX in lipid emulsions can markedly inhibit the proliferation of HCT116 human colorectal cancer cells (52). Further evaluations by Alfaifi *et al* (35) explored the cytotoxic potential of FBX-PLGA-PEG nanoparticles in A549, whilst Burmaoglu *et al* (53) reported that novel XO inhibitors can markedly reduce the viability of breast cancer cells MCF-7 and colon cancer cells Caco-2. The present study corroborated with these aforementioned findings, confirming that FBX can exert potent cytotoxicity in NSCLC by inhibiting XOR activity. In addition, it was hypothesized that the FBX-mediated reduction in NSCLC cell viability may primarily reflect impaired proliferation rather than apoptosis alone, as the modest increase in

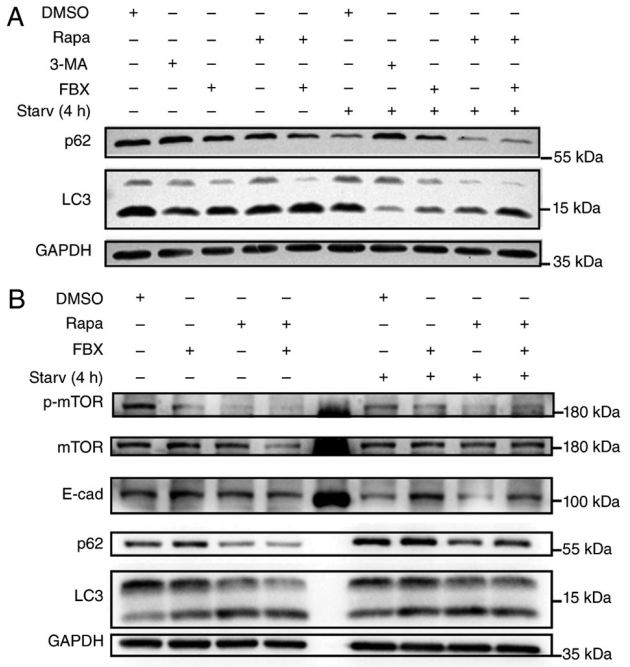


Figure 6. Rapamycin neutralized the effect of FBX on autophagy of non-small cell lung cancer cells. (A) The expression levels of p62 and LC3 proteins in A549 cells pre-treated with FBX, 3-MA and Rapa were analyzed by western blotting. (B) The levels of p-mTOR, mTOR, E-cad, p62 and LC3 proteins in SK-MES-1 cells pre-treated with FBX and Rapa were analyzed by western blotting. Rapa, rapamycin; FBX, febuxostat; Cad, cadherin; p-, phosphorylated; 3-MA, 3-methyladenine; Starv, starvation.

apoptotic rate shown in Fig. 2D cannot fully account for the ~50% cytotoxic effect observed.

To the best of our knowledge, the present study provided the first evidence that FBX can significantly diminish the migratory and invasive abilities of NSCLC cells. Although FBX significantly impaired NSCLC cell proliferation, which could potentially confound longer-term wound healing assays, this proliferative difference is negligible in short-term Transwell invasion experiments (<24 h), where equal cell numbers are seeded. According to pharmacokinetic studies of FBX (54), single doses of 40, 80 and 120 mg achieve peak plasma concentrations of 1.6-2.8, 2.6-5.0 and 4.8-7.7 μg/ml, respectively, corresponding to 5-8.8, 8.2-17 and 15-24 μM. Multiple-dose regimens showed no serious adverse events or drug accumulation, demonstrating good tolerability in humans (55). These concentrations are comparable with those used in the present *in vitro* experiments, suggesting theoretical feasibility. However, to the best of our knowledge, no clinical reports have yet described the use of FBX or other XOR inhibitors in patients with NSCLC.

Wang *et al* (32) first established that exogenous XO can trigger autophagy in A549 cells. The present database analysis corroborates this by demonstrating a positive correlation between XO expression and early autophagic regulators, including BECN1 and ATG5, in addition to the lysosomal marker LAMP2, in patients with lung cancer. Consequently, it was hypothesized that FBX can attenuate autophagic flux in NSCLC cells by inhibiting XOR enzymatic activity. Western blot analysis confirmed that FBX differentially attenuates autophagy in NSCLC cells. Under short-term (4 h) starvation, FBX suppressed LC3-II formation in A549 cells, indicating reduced mature autophagosome biogenesis, whereas this effect was absent in SK-MES-1 cells. Notably, p62 accumulated in both cell lines, suggesting that FBX primarily blocks autophagic degradation in SK-MES-1 cells, whilst in A549 cells it may additionally inhibit autophagosome formation. This differential inhibition became more pronounced following prolonged (24 h) starvation. These differential effects suggest that FBX may impede distinct stages of autophagy. Furthermore, the differential rescue effects were evident in cell viability assays. Co-treatment with Rapa and FBX restored A549 cell viability nearly to control levels, whereas only partial rescue was observed in SK-MES-1 cells. This further suggests that FBX may exclusively block autophagic degradation in LUSC cells, while in LUAD cells it additionally impairs autophagosome formation, a function specifically reversed by Rapa. It is well established that the accumulation of ROS within cells and mitochondria serves as a potent stimulus for autophagy through the canonical AMPK/mTOR/Unc51-like kinase (ULK1) pathway (56). Wang *et al* (57) reported that allopurinol can inhibit XOR, thereby blocking gemcitabine-induced phosphorylation of TGFβ-activated kinase 1 (TAK1), JNK, AMPK and ULK1, suppressing gemcitabine-triggered autophagy and enhancing gemcitabine cytotoxicity in HeLa and HT-29 cells. Therefore, FBX may similarly inhibit autophagy through these pathways (58).

It is well established that XO generates superoxide anion and hydrogen peroxide (H_2O_2) as byproducts during its catalytic cycle. FBX-mediated XOR inhibition attenuates ROS production, thereby conferring cyto-protection (59). Huang *et al* (60) previously demonstrated that inhibiting cathepsin S can trigger autophagy and subsequently upregulate XO expression and activity, leading to ROS-mediated DNA damage and cell death. In that model, XO blockade did abrogate ROS production but did not prevent autophagy activation. By contrast, the present findings indicate that FBX treatment can induce a rapid increase in intracellular ROS and subsequently inhibit autophagy in NSCLC cells. Comparable findings were observed in bladder cancer (61), where combined FBX and 5-aminolevulinic acid (5-ALA) treatment markedly enhanced ROS generation relative to 5-ALA monotherapy. Pretreatment with NAC abrogated FBX-mediated ROS production and subsequently ameliorated cell viability, indicating that ROS contributes to the FBX-induced cytotoxic effect. Emerging evidence (62,63) preliminarily suggests a complex reciprocal regulatory relationship between XOR and ROS; however, the precise source of ROS remains elusive.

Beyond the modulation of autophagy, the anti-tumor efficacy of FBX may be governed by the functional balance between XO and XDH. The natural compound Alternol has been found to enhance the oxidative activity of XDH, thereby inducing apoptosis in malignant cells (63). Furthermore, Kusano *et al* (62) observed that colorectal cancer and melanoma cells progressed more rapidly in $XO^{-/-}$ mouse models compared with in $XDH^{-/-}$ or wild-type cohorts. This accelerated growth was associated with macrophages-derived ROS, since those in $XO^{-/-}$ mice exhibited higher ROS levels, which promoted the expansion of regulatory T cells in the TME. Notably, macrophage depletion markedly attenuated tumor progression. Hypoxia upregulates XOR activity and shifts the

enzyme toward its oxidase form, rendering XO the predominant source of ROS, primarily hydrogen peroxide, during hypoxia and reoxygenation (64). Collectively, these findings reinforce the hypothesis that targeted inhibition of XO activity represents a viable therapeutic strategy for managing tumor growth, especially in hypoxia conditions.

The present study has several limitations that warrant future improvement. Cell proliferation assays (such as EdU staining) should be performed to determine whether FBX primarily suppresses proliferation, whereas classical apoptotic markers [cleaved caspase-3, cleaved poly (ADP-ribose) polymerase or BAX/BCL-2 ratio] should be assessed to investigate whether FBX can induces programmed cell death. Genetic approaches, such as knockdown or rescue of key autophagy genes (such as *ATG5, ATG7* or *BECN1*) are needed to validate FBX-mediated autophagy modulation. In addition, signaling pathway components, including p-mTOR, p-AMPK, p-ULK1, p-TAK1 and p-JNK, should be examined to elucidate the molecular mechanism underlying FBX-induced autophagy. Primary NSCLC cells or patient-derived xenograft models should also be employed, with *in vivo* experiments conducted to further validate the roles and mechanisms of XOR and FBX in NSCLC. EMT markers, including N-cadherin, Vimentin, Snail, Slug, ZEB1, MMP2 and MMP9, should be assessed to clarify FBX-mediated EMT suppression. Ferroptosis markers should be examined to explore whether ferroptosis can contribute to the anti-tumor effects of FBX.

In summary, the present findings demonstrated that XOR inhibition can suppress NSCLC cell viability and invasion/migration by disrupting pro-survival autophagy. The observation that rapamycin-mediated autophagy activation effectively abrogates the anti-proliferative effects of FBX further confirms the mechanistic dependency on this pathway. Collectively, these data identify XOR participates in the metabolic regulation of lung cancer progression and suggest that XOR-targeted therapies warrant further evaluation as a novel strategy for the treatment of NSCLC.

Acknowledgements

The authors would like to acknowledge Professor Lin WenChu (Longgang District People's Hospital of Shenzhen, Shenzhen, China) for critically refining the logical structure and Dr Jia Liu (Longgang District People's Hospital of Shenzhen, Shenzhen, China) for inspiring the initial conceptual framework of the present study. In addition, the authors would like to thank Dr Celina Juliano (PhD; Faculty of College of Biological Science, University of California, Davis, USA) for editing the language.

Funding

The present study was funded by the Longgang Medical and Health Science and Technology Project (grant no. LGKCYLWS2020045).

Availability of data and materials

The data generated in the present study may be requested from the corresponding author.

Authors' contributions

XHY contributed to the study methodology (development and design of experimental procedures), performed validation (verification of experimental results) and investigation (conducting the experiments), wrote the original draft (preparation of the initial manuscript), and participated in review and editing (critical revision of the manuscript). MS and YWX performed formal analysis (statistical and computational analysis of data) and data curation (management, organization and maintenance of research data). XHY and MS confirm the authenticity of all the raw data. All authors read and approved the final version of the manuscript.

Ethical approval and consent to participate

Not applicable.

Patient consent for publication

Not applicable.

Competing interests

The authors declare that they have no competing interests.

References

1. Bray F, Laversanne M, Sung H, Ferlay J, Siegel RL, Soerjomataram I and Jemal A: Global cancer statistics 2022: GLOBOCAN estimates of incidence and mortality worldwide for 36 cancers in 185 countries. CA Cancer J Clin 74: 229-263, 2024.
2. Herbst RS, Morgensztern D and Boshoff C: The biology and management of non-small cell lung cancer. Nature 553: 446-454, 2018.
3. Goldstraw P, Chansky K, Crowley J, Rami-Porta R, Asamura H, Eberhardt WE, Nicholson AG, Groome P, Mitchell A, Bolejack V, *et al*: The IASLC lung cancer staging project: Proposals for revision of the TNM stage groupings in the forthcoming (Eighth) edition of the TNM classification for lung cancer. J Thorac Oncol 11: 39-51, 2016.
4. Duma N, Santana-Davila R and Molina JR: Non-Small cell lung cancer: Epidemiology, screening, diagnosis, and treatment. Mayo Clin Proc 94: 1623-1640, 2019.
5. Imyanitov EN, Iyevleva AG and Levchenko EV: Molecular testing and targeted therapy for non-small cell lung cancer: Current status and perspectives. Crit Rev Oncol Hematol 157: 103194, 2021.
6. Clarke MA, Barker CG, Nicholls A, Handler MP, Pickard L, Shah AZ, Walter D, De Braekeleer E, Banerji U, Choudhary JS, *et al*: Virtual tumors enable prediction of personalized therapeutic combinations for Non-small cell lung cancer. Cancer Res 86: 4705-4722, 2026.
7. He L, Zhang J, Zhao J, Ma N, Kim SW, Qiao S and Ma X: Autophagy: The last defense against cellular nutritional stress. Adv Nutr 9: 493-504, 2018.
8. Rao S, Yang H, Penninger JM and Kroemer G: Autophagy in non-small cell lung carcinogenesis: A positive regulator of antitumor immunosurveillance. Autophagy 10: 529-531, 2014.
9. Rao S, Tortola L, Perlot T, Wirnsberger G, Novatchkova M, Nitsch R, Sykacek P, Frank L, Schramek D, Komnenovic V, *et al*: A dual role for autophagy in a murine model of lung cancer. Nat Commun 5: 3056, 2014.
10. Wang J, Liu D, Sun Z, Ye T, Li J, Zeng B, Zhao Q and Rosie Xing H: Autophagy augments the self-renewal of lung cancer stem cells by the degradation of ubiquitinated p53. Cell Death Dis 12: 98, 2021.
11. Guo JY and White E: Autophagy is required for mitochondrial function, lipid metabolism, growth, and fate of KRAS(G12D)-driven lung tumors. Autophagy 9: 1636-1638, 2013.

12. Strohecker AM, Guo JY, Karsli-Uzunbas G, Price SM, Chen GJ, Mathew R, McMahon M and White E: Autophagy sustains mitochondrial glutamine metabolism and growth of BrafV600E-driven lung tumors. Cancer Discov 3: 1272-1285, 2013.
13. Guo JY, Karsli-Uzunbas G, Mathew R, Aisner SC, Kamphorst JJ, Strohecker AM, Chen G, Price S, Lu W, Teng X, *et al*: Autophagy suppresses progression of K-ras-induced lung tumors to oncocytomas and maintains lipid homeostasis. Genes Dev 27: 1447-1461, 2013.
14. Bustos SO, Antunes F, Rangel MC and Chammas R: Emerging autophagy functions shape the tumor microenvironment and play a role in cancer progression-Implications for Cancer Therapy. Front Oncol 10: 606436, 2020.
15. Chavez-Dominguez R, Perez-Medina M, Lopez-Gonzalez JS, Galicia-Velasco M and Aguilar-Cazares D: The double-edge sword of autophagy in cancer: From tumor suppression to Pro-tumor activity. Front Oncol 10: 578418, 2020.
16. Yan Y, Chen X, Wang X, Zhao Z, Hu W, Zeng S, Wei J, Yang X, Qian L, Zhou S, *et al*: The effects and the mechanisms of autophagy on the cancer-associated fibroblasts in cancer. J Exp Clin Cancer Res 38: 171, 2019.
17. Alizadeh J, Glogowska A, Thliveris J, Kalantari F, Shojaei S, Hombach-Klonisch S, Klonisch T and Ghavami S: Autophagy modulates transforming growth factor beta 1 induced epithelial to mesenchymal transition in non-small cell lung cancer cells. Biochim Biophys Acta Mol Cell Res 1865: 749-768, 2018.
18. Ren Y, Cao L, Wang L, Zheng S, Zhang Q, Guo X, Li X, Chen M, Wu X, Furlong F, *et al*: Autophagic secretion of HMGB1 from cancer-associated fibroblasts promotes metastatic potential of non-small cell lung cancer cells via NFκB signaling. Cell Death Dis 12: 858, 2021.
19. TA AL: Deciphering the role of TMEM164 in autophagy-mediated ferroptosis and immune modulation in non-small cell lung cancer. Cell Immunol 409-410: 104915, 2025.
20. Wu H, Ren J, Gong Z, Zhang Y, Zhang H, Chen W, Zhao C and Fang T: Exploring relationships between tumor mutation burden with immunity and prognosis in lung adenocarcinoma based on weighted gene co-expression network analysis. Precision Med Sci 14: 168-180, 2025.
21. Wu R, Kadier K, Xu S, Yuan P, Yang Y, Xu P, Huang X, Zhou S, Guo SB, Zhang H, *et al*: Mapping heterogeneous molecular subtypes of circadian misalignment underlying lung adenocarcinoma risk. Life Conflux 1: e137, 2025.
22. Harrison R: Structure and function of xanthine oxidoreductase: Where are we now? Free Radic Biol Med 33: 774-797, 2002.
23. Harrison R: Physiological roles of xanthine oxidoreductase. Drug Metab Rev 36: 363-375, 2004.
24. Pacher P, Nivorozhkin A and Szabo C: Therapeutic effects of xanthine oxidase inhibitors: Renaissance half a century after the discovery of allopurinol. Pharmacol Rev 58: 87-114, 2006.
25. Aslan M, Ryan TM, Adler B, Townes TM, Parks DA, Thompson JA, Tousson A, Gladwin MT, Patel RP, Tarpey MM, *et al*: Oxygen radical inhibition of nitric oxide-dependent vascular function in sickle cell disease. Proc Natl Acad Sci USA 98: 15215-15220, 2001.
26. Enroth C, Eger BT, Okamoto K, Nishino T, Nishino T and Pai EF: Crystal structures of bovine milk xanthine dehydrogenase and xanthine oxidase: Structure-based mechanism of conversion. Proc Natl Acad Sci USA 97: 10723-10728, 2000.
27. Berry CE and Hare JM: Xanthine oxidoreductase and cardiovascular disease: Molecular mechanisms and pathophysiological implications. J Physiol 555: 589-606, 2004.
28. Filomeni G, De Zio D and Cecconi F: Oxidative stress and autophagy: The clash between damage and metabolic needs. Cell Death Differ 22: 377-388, 2015.
29. Gao Q: Oxidative stress and autophagy. Adv Exp Med Biol 1206: 179-198, 2019.
30. Kaynar H, Meral M, Turhan H, Keles M, Celik G and Akcay F: Glutathione peroxidase, glutathione-S-transferase, catalase, xanthine oxidase, Cu-Zn superoxide dismutase activities, total glutathione, nitric oxide, and malondialdehyde levels in erythrocytes of patients with small cell and non-small cell lung cancer. Cancer Lett 227: 133-139, 2005.
31. Kim AW, Batus M, Myint R, Fidler MJ, Basu S, Bonomi P, Faber LP, Wightman SC, Warren WH, McIntire M, *et al*: Prognostic value of xanthine oxidoreductase expression in patients with non-small cell lung cancer. Lung Cancer 71: 186-190, 2011.
32. Wang X, Li Y, Liu D, Wang Y and Ming H: Astragalus polysaccharide inhibits autophagy and regulates expression of autophagy-related proteins in lung cancer A549 cells induced by xanthine oxidase. Xi Bao Yu Fen Zi Mian Yi Xue Za Zhi 35: 619-624, 2019 (In Chinese).
33. Tayar JH, Lopez-Olivo MA and Suarez-Almazor ME: Febuxostat for treating chronic gout. Cochrane Database Syst Rev 11: CD008653, 2012.
34. Joshi G, Sharma M, Kalra S, Gavande NS, Singh S and Kumar R: Design, synthesis, biological evaluation of 3,5-diaryl-4,5-dihydro-1H-pyrazole carbaldehydes as non-purine xanthine oxidase inhibitors: Tracing the anticancer mechanism via xanthine oxidase inhibition. Bioorg Chem 107: 104620, 2021.
35. Alfaifi MY, Shati AA, Elbehairi SEI, Fahmy UA, Alhakamy NA and Md S: Anti-tumor effect of PEG-coated PLGA nanoparticles of febuxostat on A549 non-small cell lung cancer cells. 3 Biotech 10: 133, 2020.
36. Livak KJ and Schmittgen TD: Analysis of relative gene expression data using real-time quantitative PCR and the 2(-Delta Delta C(T)) method. Methods 25: 402-408, 2001.
37. Yu L, McPhee CK, Zheng L, Mardones GA, Rong Y, Peng J, Mi N, Zhao Y, Liu Z, Wan F, *et al*: Termination of autophagy and reformation of lysosomes regulated by mTOR. Nature 465: 942-946, 2010.
38. Konno H, Minamiya Y, Saito H, Imai K, Kawaharada Y, Motoyama S and Ogawa J: Acquired xanthine dehydrogenase expression shortens survival in patients with resected adenocarcinoma of lung. Tumour Biol 33: 1727-1732, 2012.
39. Liu H, Zhu H, Shi W, Lin Y, Ma G, Tao G, Gong W, Zhao Q, Du M, Wang M, *et al*: Genetic variants in XDH are associated with prognosis for gastric cancer in a Chinese population. Gene 663: 196-202, 2018.
40. Chen MM, Guo W, Chen SM, Guo XZ, Xu L, Ma XY, Wang YX, Xie C and Meng LH: Xanthine dehydrogenase rewires metabolism and the survival of nutrient deprived lung adenocarcinoma cells by facilitating UPR and autophagic degradation. Int J Biol Sci 19: 772-788, 2023.
41. Hair PI, McCormack PL and Keating GM: Febuxostat. Drugs 68: 1865-1874, 2008.
42. White EZ, Pennant NM, Carter JR, Hawsawi O, Odero-Marah V and Hinton CV: Serum deprivation initiates adaptation and survival to oxidative stress in prostate cancer cells. Sci Rep 10: 12505, 2020.
43. Carretero-Fernández M, Cabrera-Serrano AJ, Sánchez-Maldonado JM, Ruiz-Durán L, Jiménez-Romera F, García-Verdejo FJ, González-Olmedo C, Cardús A, Díaz-Beltrán L, Gutiérrez-Bautista JF, *et al*: Autophagy and oxidative stress in solid tumors: Mechanisms and therapeutic opportunities. Crit Rev Oncol Hematol 212: 104820, 2025.
44. Wu YT, Tan HL, Shui G, Bauvy C, Huang Q, Wenk MR, Ong CN, Codogno P and Shen HM: Dual role of 3-methyladenine in modulation of autophagy via different temporal patterns of inhibition on class I and III phosphoinositide 3-Kinase. J Biol Chem 285: 10850-10861, 2010.
45. Jiang P and Mizushima N: LC3- and p62-based biochemical methods for the analysis of autophagy progression in mammalian cells. Methods 75: 13-18, 2015.
46. Aydemir S, Yildirim Z, Bara B, Dogan E and Bozok V: Differential regulation of STING expression and cisplatin sensitivity by autophagy in non-small cell lung cancer cells. Med Oncol 42: 227, 2025.
47. Han JH, Kim YK, Kim H, Lee J, Oh MJ, Kim SB, Kim M, Kim KH, Yoon HJ, Lee MS, *et al*: Snail acetylation by autophagy-derived acetyl-coenzyme A promotes invasion and metastasis of KRAS-LKB1 co-mutated lung cancer cells. Cancer Commun (Lond) 42: 716-749, 2022.
48. Takai M, Yamauchi T, Fujita K, Lee S, Ookura M, Kishi S, Urasaki Y, Yoshida A, Iwasaki H and Ueda T: Controlling serum uric acid using febuxostat in cancer patients at risk of tumor lysis syndrome. Oncol Lett 8: 1523-1527, 2014.
49. Tamura K, Kawai Y, Kiguchi T, Okamoto M, Kaneko M, Maemondo M, Gemba K, Fujimaki K, Kirito K, Goto T, *et al*: Efficacy and safety of febuxostat for prevention of tumor lysis syndrome in patients with malignant tumors receiving chemotherapy: A phase III, randomized, multi-center trial comparing febuxostat and allopurinol. Int J Clin Oncol 21: 996-1003, 2016.
50. Konishi M, Pelgrim L, Tschirner A, Baumgarten A, von Haehling S, Palus S, Doehner W, Anker SD and Springer J: Febuxostat improves outcome in a rat model of cancer cachexia. J Cachexia Sarcopenia Muscle 6: 174-180, 2015.

51. Oh SH, Choi SY, Choi HJ, Ryu HM, Kim YJ, Jung HY, Cho JH, Kim CD, Park SH, Kwon TH and Kim YL: The emerging role of xanthine oxidase inhibition for suppression of breast cancer cell migration and metastasis associated with hypercholesterolemia. FASEB J 33: 7301-7314, 2019.
52. Fahmy UA, Aldawsari HM, Badr-Eldin SM, Ahmed OAA, Alhakamy NA, Alsulimani HH, Caraci F and Caruso G: The encapsulation of febuxostat into emulsomes strongly enhances the cytotoxic potential of the drug on HCT 116 colon cancer cells. Pharmaceutics 12: 965, 2020.
53. Burmaoglu S, Ozcan S, Balcioglu S, Gencel M, Noma SAA, Essiz S, Ates B and Algul O: Synthesis, biological evaluation and molecular docking studies of bis-chalcone derivatives as xanthine oxidase inhibitors and anticancer agents. Bioorg Chem 91: 103149, 2019.
54. Luo Z, Nan F, Miao J, Chen Z, Li M and Liang M: Pharmacokinetics and bioequivalence of two formulations of febuxostat 40-Mg and 80-Mg tablets: A randomized, open-label, 4-Way crossover study in healthy Chinese male volunteers. PLoS One 11: e0150661, 2016.
55. Jordan A and Gresser U: Side effects and interactions of the xanthine oxidase inhibitor febuxostat. Pharmaceuticals (Basel) 11: 51, 2018.
56. Poillet-Perez L, Despouy G, Delage-Mourroux R and Boyer-Guittaut M: Interplay between ROS and autophagy in cancer cells, from tumor initiation to cancer therapy. Redox Biol 4: 184-192, 2015.
57. Wang J, Hu Y, Liu P and Xu X: Xanthine oxidoreductase mediates genotoxic drug-induced autophagy and apoptosis resistance by uric acid accumulation and TGF-β-activated kinase 1 (TAK1) activation. FASEB J 37: e22723, 2023.
58. Wang Y, Lu X, Tan J, He J, Yin H, Chen P, Wu H, Luo Y and Li M: The cGAS-STING pathway: Insights into regulatory mechanisms, disease dysregulation, and therapeutic development. Life Conflux 2: e300, 2025.
59. Fukui T, Maruyama M, Yamauchi K, Yoshitaka S, Yasuda T and Abe Y: Effects of febuxostat on oxidative stress. Clin Ther 37: 1396-1401, 2015.
60. Huang CC, Chen KL, Cheung CHA and Chang JY: Autophagy induced by cathepsin S inhibition induces early ROS production, oxidative DNA damage, and cell death via xanthine oxidase. Free Radic Biol Med 65: 1473-1486, 2013.
61. Khatami F, Sharifkazemi H, Taheri D, Oskouie IM, Mirzaei A, Mashhadi R, Nikoofar P and Aghamir SMK: Evaluating the impact of febuxostat on 5-Aminolevulinic Acid-based photodynamic therapy in bladder cancer cell lines. Photodiagnosis Photodyn Ther 56: 105286, 2025.
62. Kusano T, Ehirchiou D, Matsumura T, Chobaz V, Nasi S, Castelblanco M, So A, Lavanchy C, Acha-Orbea H, Nishino T, *et al*: Targeted knock-in mice expressing the oxidase-fixed form of xanthine oxidoreductase favor tumor growth. Nat Commun 10: 4904, 2019.
63. Xu H, Li C, Mozziconacci O, Zhu R, Xu Y, Tang Y, Chen R, Huang Y, Holzbeierlein JM, Schöneich C, *et al*: Xanthine oxidase-mediated oxidative stress promotes cancer cell-specific apoptosis. Free Radic Biol Med 139: 70-79, 2019.
64. Griguer CE, Oliva CR, Kelley EE, Giles GI, Lancaster JR Jr and Gillespie GY: Xanthine oxidase-dependent regulation of hypoxia-inducible factor in cancer cells. Cancer Res 66: 2257-2263, 2006.

Copyright © 2026 Yao et al. This work is licensed under a Creative Commons Attribution-NonCommercial-NoDerivatives 4.0 International (CC BY-NC-ND 4.0) License.